ACS APPLIED MATERIALS & INTERFACES

Research Article

www.acsami.org

Controllable Formation of (004)-Orientated Nb:TiO_2 for High-Performance Transparent Conductive Oxide Thin Films with Tunable Near-Infrared Transmittance

Xiaoyang Yang,[†] Ming-Jian Zhang,[†] Yuxin Min,[†] Ming Xu,[†] Zongwei Mei,[†] Jun Liang,*[,†] Jiangtao Hu,[†] Sheng Yuan,[†] Shu Xiao,[†] Yandong Duan,[†] Fusheng Liu,[‡] Hai Lin,[†] Yuan Lin,[†] and Feng Pan*[,†]

[†]School of Advanced Materials, Peking University Shenzhen Graduate School, 2199 Lishui Road, Shenzhen 518055, P. R. China

[‡]College of Materials Science and Engineering, Shenzhen University, 3688 Nanhai Road, Shenzhen 518060, P. R. China

Supporting Information

ABSTRACT: A niobium-doped titanium dioxide (Nb:TiO_2, NTO) film is a promising candidate material for indium-free transparent conductive oxide (TCO) films. It is challenging and interesting to control (004)-oriented growth to decrease resistivity. In this work, NTO films with different fractions of preferential (004) orientation ($\eta_{(004)}$) were controllably prepared by direct current sputtering. Notably, the direction of local-ordering of ions-packing could be adjusted by slightly changing the angle between the sputtering source and the glass substrate, which is identified as a key factor to determine the growth direction of a columnar crystal as well as the $\eta_{(004)}$ of films. Hall effect measurements indicate that NTO films with the highest $\eta_{(004)}$ present the lowest resistivity (6.4×10^{-4} Ω cm), which originates from super-high carrier concentration (2.9×10^{21} cm^{-3}) and mobility (3.4 cm^2 V^{-1} s^{-1}). The corresponding low sheet resistance (10.3 Ω sq^{-1}) makes it a potential material for commercial TCO films. We also observe that films with higher $\eta_{(004)}$ show lower transmittance in the near-infrared region.

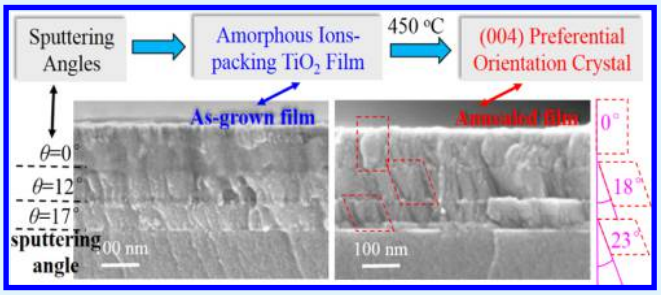

KEYWORDS: *titanium dioxide, transparent conductive oxide, thin films, preferential orientation, direct current sputtering*

INTRODUCTION

With the development of optoelectronic and photovoltaic devices, wide-bandgap transparent conductive oxide (TCO) thin films have attracted increasing attention due to their salient advantages of optical transparency and electrical conductivity.[1−4] The tin-doped indium oxide (ITO) is the most frequently used material in practical TCO thin films. However, the rare indium makes it difficult to meet the increasing demand for TCO films.[5−7] Niobium-doped anatase TiO_2 (NTO) is of rich abundance, environmentally friendly, and chemically stable at high temperatures, as well as in acids and alkalis.[8−13] In addition, NTO shows high transmittance in the visible region and exhibits a low resistivity of $2-3 \times 10^{-4}$ Ω cm in the epitaxial thin-film form.[14] Therefore, NTO could be a promising candidate material for indium-free TCO thin films.

NTO thin films have been successfully fabricated by various techniques, including pulsed laser deposition (PLD),[14−16] magnetron sputtering (MS),[9,11,17−24] atomic layer deposition,[25] aerosol-assisted chemical vapor deposition,[10] and sol−gel method.[26,27] Table S1 shows the reported high conductivity of NTO thin films on the basis of different deposition techniques. Among these techniques, thin films from PLD and reactive sputtering show lower resistivity than those from others. However, PLD has not yet been widely applied because of its high cost and the small area of NTO films. The sputtering technique is inexpensive and has feasibility in large-area fabrication, but reactive sputtering often has a problem of target poisoning because of chemical reactions.[28−30] Therefore, direct current (DC) sputtering with a conductive oxide target becomes a good choice.

The high conductivity of NTO films is critically related to the crystal phase and crystalline orientation. For example, the rutile phase can suppress the percolative conduction of anatase films and hence the formation of a mixed crystal phase must be avoided.[20] In addition, Hirose et al. showed that NTO films of (001)-oriented growth show lower resistivity than that of (100)-oriented growth due to high electron mobility.[11,31] Therefore, preparation of anatase NTO thin films with (001)-oriented growth is an effective way for increasing conductivity. However, according to the thermodynamics, (001) orientation is unstable because of its higher surface free energy than that of (101) orientation.[32] Therefore, achieving preferential (004) growth is difficult, and methods based on growth kinetics should be used. The epitaxial technique and the method of predepositing a seed layer are usually used but are not suitable for large-area fabrication.[11,14,33] To our knowledge, there is no other method

Received: May 14, 2017
Accepted: August 9, 2017
Published: August 9, 2017

DOI: 10.1021/acsami.7b06792
ACS Appl. Mater. Interfaces XXXX, XXX, XXX−XXX

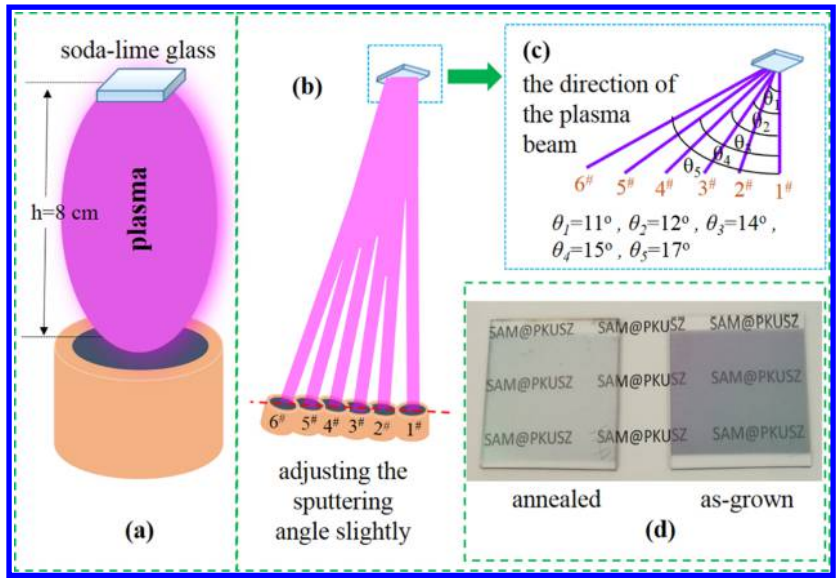

Figure 1. (a) Schematic of NTO thin film preparation via a normal DC sputtering. (b) Diagram of adjusting the sputtering angle for preparation. (c) Comparison of the direction of the plasma beam before and after adjusting the sputtering angle. (d) Photographs of as-grown and annealed NTO thin films on a glass substrate.

reported to control (001)-oriented growth on an amorphous substrate for conductive NTO thin films in present researches. So it is still a great challenge to implement the controllable crystalline orientation on an amorphous substrate for NTO thin films.

For TiO_2 thin films, some efforts have made by reactive sputtering. Stefanov et al. found that a relatively high partial pressure of O_2 is important to control preferred (004) orientation.[34] They achieved a maximum fraction of preferential (004) orientation ($\eta_{(004)}$) of 39% for TiO_2 thin films. However, this method is unsuitable for DC sputtering with a conductive oxide target. Zheng et al. prepared TiO_2 thin films with a dominated (004) peak in the X-ray diffraction (XRD) pattern using high sputtering power and a sputtering angle of 37°.[35] However, these thin films consisted of the anatase−rutile mixed phase. We deduce that adjusting the sputtering angle will be an optimal choice, if the mixed phase can be avoided. In previous studies, preferred orientations are often observed in a glancing-angle deposition technique (the sputtering angle is usually large).[36−41] The preferred orientation originates from orientated growth of the columnar crystal toward the direction of the vapor or plasma beam, which competes with thermodynamics. However, not crystal but amorphous thin films are formed when a low sputtering power is used to avoid the anatase−rutile mixed phase.[42] Now what matters is whether the ions-packing is following the direction of the plasma beam in amorphous thin films.

In this work, we report for the first time the formation of anatase NTO films with controllable $\eta_{(004)}$ by adjusting the DC sputtering angle slightly. The formation of preferential (004) orientation is closely related to local-ordering of ions-packing in amorphous as-grown films. The scanning electron microscope (SEM) analysis shows direct evidence of local-ordering of ions-packing having a specific direction during sputtering, when there is an angle between the sputtering source and the glass substrate. After annealing, NTO films with the maximum $\eta_{(004)}$ (38.7%) show the lowest resistivity (6.4×10^{-4} Ω cm), which originates from super-high carrier concentration (2.9×10^{21} cm^{-3}) and mobility (3.4 cm^2 V^{-1} s^{-1}). The conductivity of NTO thin films becomes better as the $\eta_{(004)}$ increases. In addition, NTO thin films show optical anisotropy as $\eta_{(004)}$ is adjusted from 10.5 to 38.7%. The films with higher $\eta_{(004)}$ show lower transmittance in the near-infrared region. This work demonstrates a new way to control the film transmittance, which is important to glass for the optical application in the near-infrared region.[43]

EXPERIMENTAL SECTION

General Film Preparation. NTO thin films were sputtered onto a 3 × 3 cm^2 soda-lime glass substrate (GULUO GLASS) using a Φ 6 cm oxide target. This target consists of 5 mol % Nb_2O_5 in TiO_2 ($Ti_{0.95}Nb_{0.05}O_2$, 99.9%, Hzamtarget). The substrate was secured with a high-temperature polyamide tape (2 mm wide) to a 6 × 6 cm^2 piece of stainless steel substrate holder. The distance was 8 cm between the center of the target and substrate. The base pressure before each deposition was 8×10^{-4} Pa. Films were deposited in pure argon (grade 5.0) at a flow rate of 20 sccm (cubic centimeter per minute at STP) and a system pressure of 0.3 Pa. The substrate temperature during deposition was 40−60 °C measured with a thermocouple. A DC sputtering power (SKY Technology Development DC power system) of 40−45 W was required to prepare films with a thickness of ∼640 nm on the soda-lime glass substrate after 1.5 h of deposition. Before each deposition, the target surface was sputter-cleaned by pure Ar for 10 min and then presputtered for 5 min under the film deposition conditions. The as-deposited films were annealed and crystallized in an Ar/H_2 (95:5, *v*/*v*) atmosphere at a flow rate of 30 sccm in a horizontal furnace at 450 °C for 30 min. The temperature was increased at a rate of 10 °C min^{-1}. Then, the films were cooled down naturally to room temperature.

In a normal DC sputtering, for example, NTO thin film 1#, the direction of the plasma beam incidence to the substrate was vertical, and the sputtering angle was considered as 0° (Figure 1a). When adjusting the sputtering angle, the plasma beam incidence to the substrate was considered as an oblique jet-flow, for example, NTO thin films 2#−6#, which had a gradient angle compared with that in the normal DC sputtering (Figure 1b). This gradient angle could be calculated from the horizontal shift of the substrate and the vertical distance (8 cm) between the target and the substrate.

Film Analysis. The crystal structure, preferred orientation growth, and residual stress of NTO films were analyzed using a Bruker D8 Advance powder X-ray diffractometer equipped with Cu Kα radiation with a two-dimensional detector. The scan range of 2θ was from 10 to 120°, and the scan step of 2θ was 0.02°. The scan time was 1 and 2 s/step

DOI: 10.1021/acsami.7b06792
ACS Appl. Mater. Interfaces XXXX, XXX, XXX−XXX

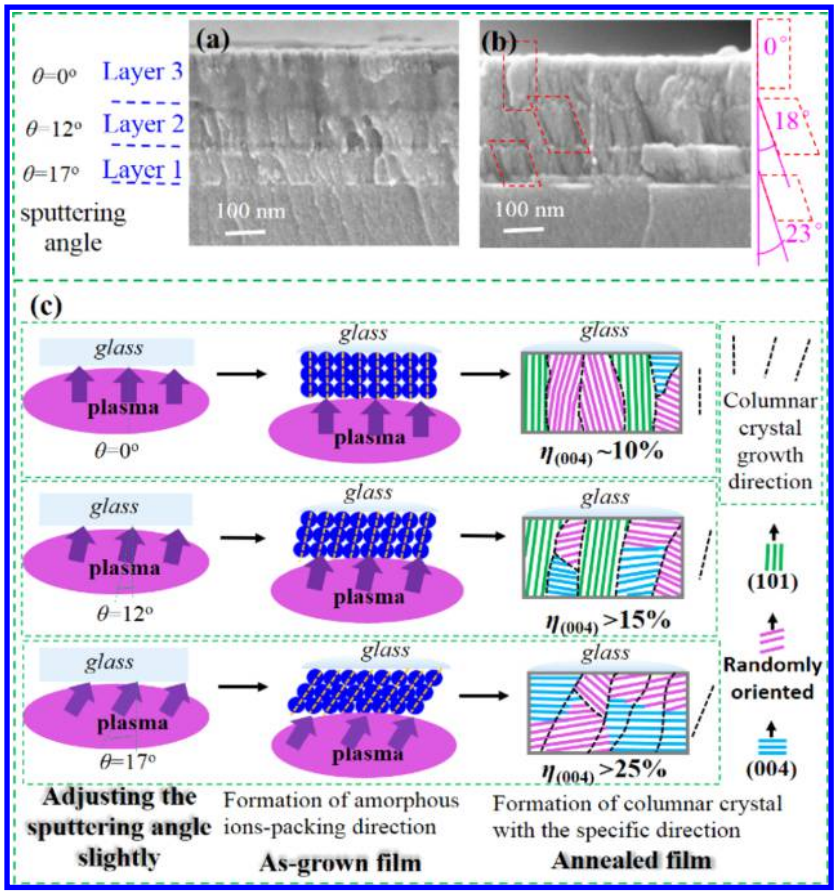

Figure 2. Side-on SEM images of (a) as-grown thin film and (b) annealed thin film. Layers 1, 2, and 3 are prepared with sputtering angles of 17, 12, and 0°, respectively. The red quadrangles indicate the columnar crystal in three layers. (c) Diagram of the formation of the NTO thin films with different $\eta_{(004)}$ values. A list of blue spheres represents ions-packing following the direction of the plasma beam.

for normal analysis and Rietveld refinement, respectively. The 1/4 Euler ring (azimuthal angle $\varphi = -90°$) was used to collect the data of 2θ ((004) peak) for the residual stress analysis. The collimator was 0.5 mm in diameter. A series of specific sample-tilting angles (Ψ values: 5, 10, 15, 20, 25, 30, 35, 40, 45, and 50°) were used for each NTO thin film.

The Le Bail analysis was used to fit the collected XRD data with total pattern solution (TOPAS) to obtain unit cell parameters, unit volume, and March−Dollase (MD) parameter for the (004) direction.

Microstructures were observed by using a JEOL JEM2010-FEF high-resolution transmission electron microscope (HRTEM). The interplanar spacing was calculated from the corresponding diffraction spots in the fast Fourier transform (FFT) algorithm images.

Electrical properties of films were measured at room temperature on an Ecopia HMS-3000 Hall effect measurement system set up in the Van der Pauw configuration. Measurements were carried out on 1 × 1 cm^2 squares, and a standard ITO sample was tested before any NTO thin film measurements.

The thickness of the films was measured using a Bruker DektakXT profilometer with a proper measurement range of 6.5 μm.

Optical transmission was analyzed over the wavelength range of 200−3300 nm using a PerkinElmer Lambda 950 ultraviolet/visible/near-infrared spectrometer. Thin films were characterized by Raman spectroscopy with a laser excitation energy of 532 nm in a Horiba iHR320 Raman spectrometer with a cooled CCD detector.

The morphology of thin films was measured using a Zeiss SUPRA-55 scanning electron microscope (SEM). The content of Nb was investigated via an Oxford-Max 20 energy dispersive spectrometer (EDS).

Photographs were taken using a camera in a Hua Wei Mate 8 mobile phone.

Degree of Preferential (004) Orientation ($\eta_{(004)}$). The degree of preferential (004) orientation could be quantified as follows

$$\eta_{(004)} = \sqrt{\frac{(1-\mathrm{MD}_{(004)})^3}{1-\mathrm{MD}_{(004)}{}^3}} \times 100\% \quad (1)$$

where $\mathrm{MD}_{(004)}$ is the March−Dollase parameter for the (004) direction and could be obtained from the Rietveld refinement.[34]

RESULTS AND DISCUSSION

Origin of Controllable Crystalline Orientation. Our thermodynamics simulation shows that the (004) orientation has higher surface free energy than the (101) orientation (Table S2). This result indicates that it is difficult to form (004) preferential growth in a normal condition. Therefore, adjusting the sputtering angle is chosen as a method to achieve this aim.

To clearly show different orientations among different sputtering angles, a special thin film was sputtered for a specified time by controlling the sputtering angle at 17, 12, and 0°, respectively. It is important to note that sputtering is continuous. In other words, sputtering is not interrupted when the sputtering angle changes. The SEM images of the as-grown NTO thin film clearly show a discernible boundary between two layers with different sputtering angles (Figure 2a). This boundary occurs due to a mismatch of ions-packing during sputtering. To our knowledge, this is the first report of a mismatch observed in a homogeneous amorphous thin film. After annealing, columnar crystal growth is observed in three layers toward different directions (Figure 2b). This result indicates that the mismatch originates from different packing directions of ions in the as-grown film during sputtering. Furthermore, the result also

DOI: 10.1021/acsami.7b06792
ACS Appl. Mater. Interfaces XXXX, XXX, XXX−XXX

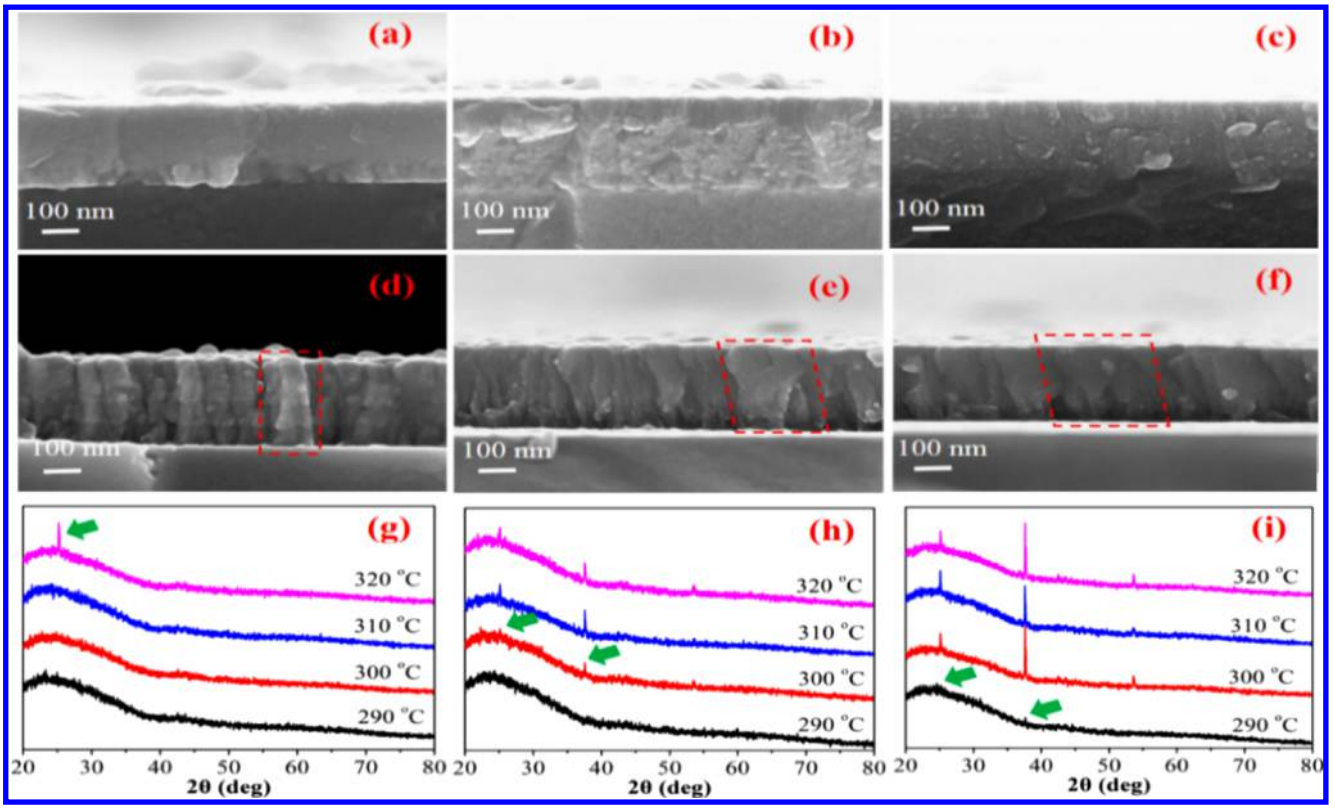

Figure 3. Side-on SEM images of as-grown NTO thin films with sputtering angles of (a) 0°, (b) 12°, and (c) 17°. Side-on SEM images of annealed NTO thin films with sputtering angles of (d) 0°, (e) 12°, and (f) 17°. The red quadrangles indicate the columnar crystal in three films. X-ray diffraction patterns of NTO thin films with sputtering angles of (g) 0°, (h) 12°, and (i) 17° with different annealing temperatures. The green arrows mark the (101) and (004) peaks, the only peaks that could be detected.

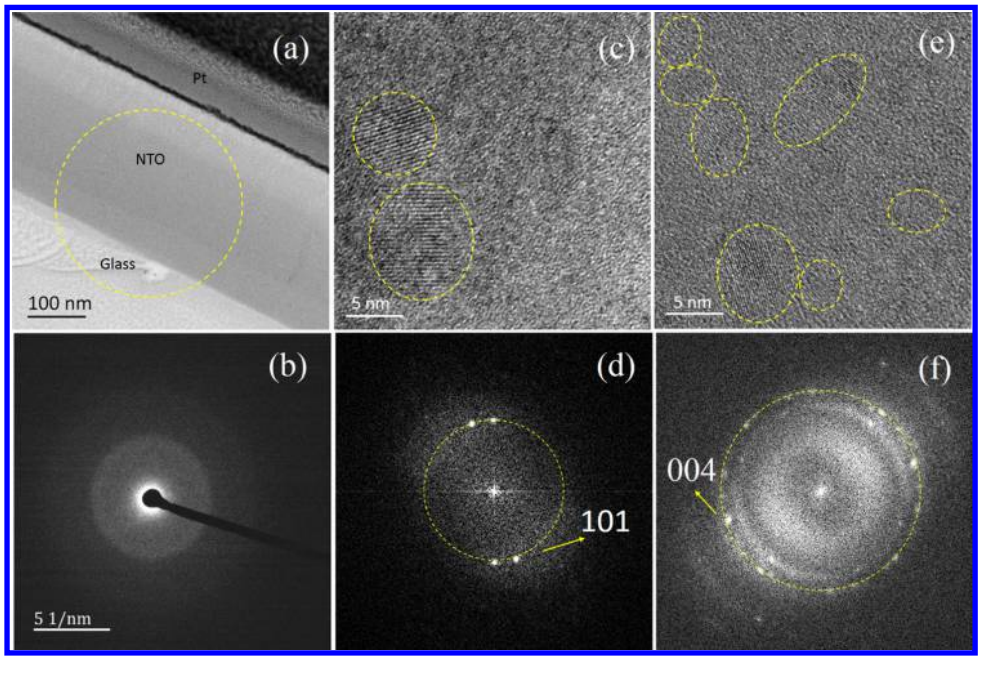

Figure 4. TEM image of as-grown NTO thin films (a) and selected area electron diffraction pattern with diffuse rings from the yellow circle region (b). HRTEM images of as-grown NTO thin films with a sputtering angle of 0° (c) and 17° (e). FFT images (d) and (f) from HRTEM images (c) and (e).

indicates that the direction of local-ordering of ions-packing can determine the growth direction of the columnar crystal. Therefore, adjusting the sputtering angle is a feasible method to form a columnar crystal following almost the same direction after annealing (Figure 2c).

We suppose a fit ions-packing could provide motivation of preferential orientation for crystal growth in kinetics. To support our hypothesis, three types of thin films are prepared with sputtering angles of 0, 12, and 17°, respectively. As-grown NTO thin films from a normal sputtering (sputtering angle of 0°) show

DOI: 10.1021/acsami.7b06792
ACS Appl. Mater. Interfaces XXXX, XXX, XXX−XXX

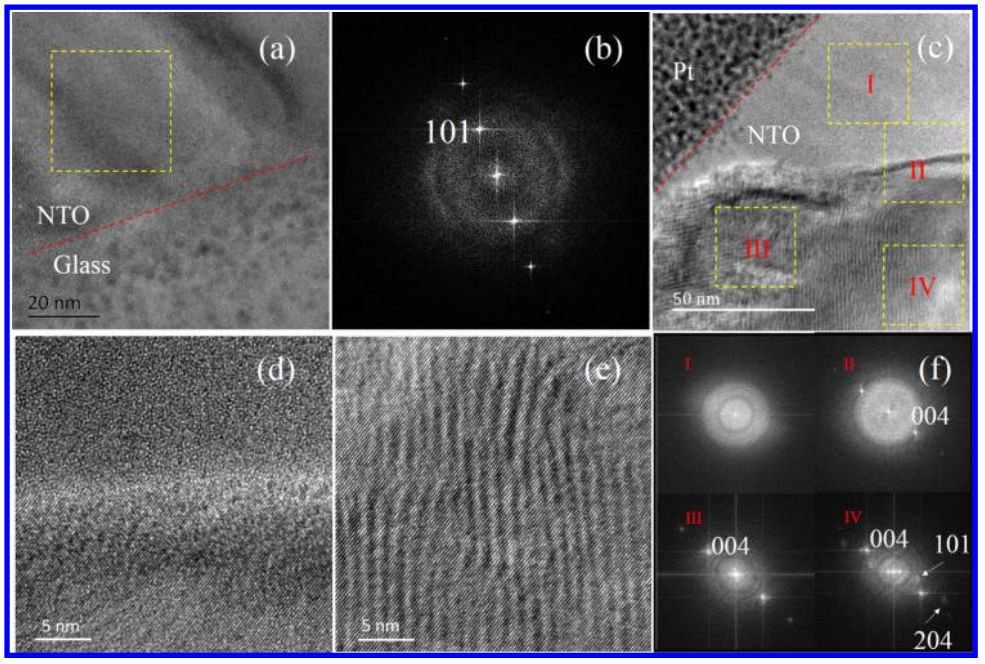

Figure 5. TEM images of annealing NTO thin films with sputtering angles of 0° (a) and 17° (c). FFT images (b) from the yellow square region in TEM image (a). HRTEM images (d) and (e) from regions II and III in the TEM image (c). FFT images I–IV (f) from regions I–IV in TEM image (c).

uniform and compact primary particle packing (Figure 3a). As-grown NTO thin films from sputtering angles of 12 and 17° show compact secondary particle packing (Figure 3b,c). We believe these differences between as-grown NTO thin films are important for the formation of the preferential orientation. As expected, annealed NTO thin films show typical columnar crystal growth following almost the same direction of the plasma beam (Figure 3d–f). This result is in good agreement with the columnar crystal in that special thin film. To analyze the influence of the stress, the residual stress of all the NTO thin films were measured via the traditional XRD method (the $\sin^2\Psi$ method).[44] The stress constant was estimated from Poisson ratio $\upsilon = 0.27$ and Young modulus $E = 150$ GPa.[45] The residual stresses are -412.1 ± 36.7, -402.9 ± 56.4, and -481.3 ± 21.4 MPa for NTO thin films prepared with sputtering angles of 0, 12, and 17°, respectively (Figurer S1 and Table S3). The trend of residual stresses is not consistent with that of the XRD results. The differences of residual stresses could be caused by the small fluctuation of the sputtering pressure and discharge current.[46,47]

The XRD data show that these NTO thin films have different $\eta_{(004)}$ values (Figure 3g–i). A typical (101) peak could be observed for NTO thin films with a sputtering angle of 0° (Figure 3g). Figure 3h,i shows that the (004) peak becomes stronger as the sputtering angle increases. This result indicates that the sputtering angle is important for crystal growth in kinetics.

The as-grown thin films are amorphous as verified by the broad diffuse rings in the electron diffraction patterns (Figure 4a,b). This result is in good agreement with our XRD analysis. Notably, some small crystalline clusters (several nanometers in size) with the anatase structure can be found in some regions of these thin films (Figure 4c,e). This phenomenon was found in the previous work.[46] These small crystalline clusters have (101) and (004) crystal planes in thin films with a sputtering angle of 0 and 17°, respectively, as shown in Figure 4d,f. The (101) and (004) crystal planes are determined from the interplanar spacing of 0.3514 and 0.2366 nm. After annealing, the preferential orientation is formed in thin films. As shown in Figure 5a,b, the (101) crystal planes are parallel to the substrate in thin films with a sputtering angle of 0°. Figure 5c–f shows the formation of preferential (004) orientation in thin films with a sputtering angle of 17°. FFT images II and III (Figure 5f) show glowing bright spots arranged in a line, indicating that the crystal region is a single crystal composed of parallel (004) planes. However, FFT image IV shows some other bright spots. The crystal planes are determined to be (101) and (204) planes from the interplanar spacing of 0.3511 and 0.1490 nm. We noticed that the angle between (004) and (101) planes was not around 68°, but the angle between (101) and (204) planes was close to 16° (calculation value: 16.8°). This result indicates that crystal region IV is part of a twin crystal. We deduce that (101) planes can be formed even though there are single crystals composed of parallel (004) planes nearby, but the (004) planes are not completely disappeared.

With the analysis above, we consider the direction of local-ordering of ions-packing as a key factor to determine the growth direction of the columnar crystal as well as the $\eta_{(004)}$ of films. In addition, (101) and (004) peaks appear at the same time in one thin film (Figure 3g–i), when different annealing temperatures are used. This result suggests that the crystalline orientation is not controlled by thermodynamics in our system.

Controllable Preparation and Identification for NTO Thin Films. NTO thin films $1^{\#}$–$6^{\#}$ were prepared with different sputtering angles (Figure 1a,b). As-grown NTO thin films of $2^{\#}$, $3^{\#}$, $4^{\#}$, $5^{\#}$, and $6^{\#}$ are achieved with sputtering angles of 11, 12, 14, 15, and 17°, respectively (Figure 1c). The as-grown NTO thin films show a transparent blue-green color, and the transmittance of thin films increases after annealing (Figure 1d). The transmittance of as-grown NTO thin films decreases with increasing $\eta_{(004)}$, as shown in Figures S2 and S3.

After annealing at 450 °C for 30 min, NTO thin films $1^{\#}$–$6^{\#}$ have different $\eta_{(004)}$ values, as listed in Table 1. The XRD data show that these NTO thin films have an anatase crystal phase (Figure 6a). It is worth noting that there is no diffraction peak of rutile or brookite phases. The XRD diffraction patterns are slightly broad and diffuse around 25° due to amorphous

DOI: 10.1021/acsami.7b06792
ACS Appl. Mater. Interfaces XXXX, XXX, XXX–XXX

Table 1. Summary of Sputtering Angle, March−Dollase (MD) Parameter, Fraction of (004) Orientation ($\eta_{(004)}$), Peak Area Ratio of (101) and (004) Peaks ((101):(004)), and Classification of Sample of NTO Thin Films $1^{\#}$−$6^{\#}$ According to the Peak Area Ratio

sample	sputtering angle (deg)	MD	$\eta_{(004)}$ (%)	(101):(004)	classification
$1^{\#}$	0	0.833	10.5	69:31	D(101)
$2^{\#}$	11	0.728	18.0	54:46	E(101)−(004)
$3^{\#}$	12	0.697	20.2	53:47	E(101)−(004)
$4^{\#}$	14	0.611	27.5	40:60	D(004)
$5^{\#}$	15	0.557	32.4	34:66	D(004)
$6^{\#}$	17	0.487	38.7	21:79	D(004)

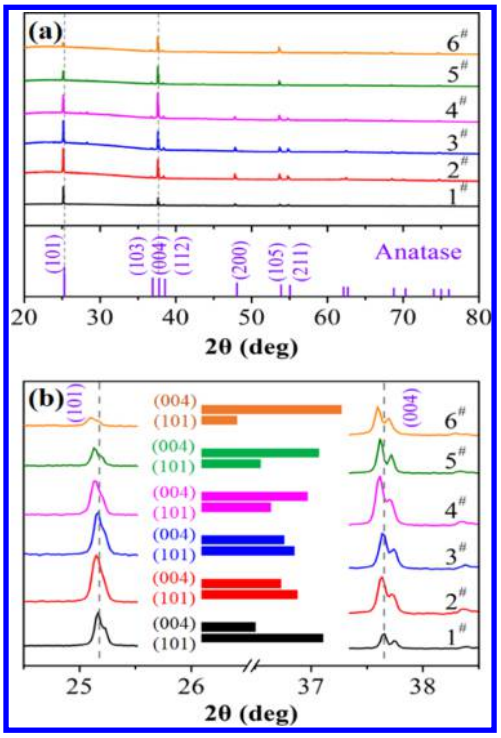

Figure 6. (a) X-ray diffraction patterns of anatase NTO thin films with different $\eta_{(004)\ values}$. $1^{\#}$, $2^{\#}$, $3^{\#}$, $4^{\#}$, $5^{\#}$, and $6^{\#}$ are prepared with sputtering angles of 0, 11, 12, 14, 15, and 17°, respectively. (b) Comparison of (101) and (004) peaks. Note the shift of (101) and (004) peaks. The histogram inset depicts the peak area ratio of (101) and (004) peaks for $1^{\#}$−$6^{\#}$.

scattering of X-rays by the glass substrate. Compared with the anatase phase of pure TiO_2 (space group: $I4_1/amd$ (141), JCPDS No. 21-1272), the XRD peak position of NTO thin films presents a little shift toward a low angle. This is attributed to the doping of Nb, because the ionic radius of Nb^{5+} (ca. 0.70 Å) is a little larger than that of Ti^{4+} (ca. 0.68 Å).

Amazingly, (101)- and (004)-oriented growth of those thin films are detected clearly by XRD. A comparison of (101) and (004) peaks is shown in Figure 6b and is given in Table 1. By a normal DC sputtering, NTO thin film $1^{\#}$ shows a dominant (101) diffraction peak (D(101)). On adjusting the sputtering angle to 11 and 12°, the (101) peak area becomes approximately equal to the (004) peak area for NTO thin films $2^{\#}$ and $3^{\#}$ (AE(101)−(004)). When the sputtering angle exceeds 14°, the intensity and the peak area of (004) surpass those of (101) for NTO thin films $4^{\#}$−$6^{\#}$ (D(004)). This result suggests a preferential growth along the *c* axis of the anatase lattice. Compared to that of the (101) peak, the intensity of the (004) peak is enhanced gradually as the sputtering angle increases, in good agreement with the above result. In addition, a slight shift toward a small angle is observed (Figure 6b). This is because unit cell parameters fluctuate slightly as the $\eta_{(004)}$ increases.

The Le Bail analysis was used to fit the XRD pattern with TOPAS to obtain unit cell parameters, unit volume, and March−Dollase parameter for the (004) direction (Figure S4). For pure TiO_2 (space group: $I4_1/amd$ (141), JCPDS No. 21-1272), the unit cell parameters are a = 3.785 Å and c = 9.514 Å. After Nb doping, both a and c increase to around 3.800 and 9.540 Å, respectively. This result is consistent with that in the paper by Furubayashi et al.[14] Unit cell parameters fluctuate slightly with the content of Nb and the proportion of the (004)-oriented growth (Table S4). The EDS data of NTO thin films reveal the content of Nb, Ti, and O, as listed in Table S4 (details are shown in Figure S5). The results show that the doping content of Nb fluctuates from 8.1 to 8.7 atom %. In addition, the content of Ti and O is nonstoichiometric. In other words, these thin films contain oxygen vacancies, which is common in TiO_2.[48−51]

The well-defined Raman spectra between 80 and 700 cm^{-1} are characteristic of the anatase phase for NTO thin films, as shown in Figure 7. All films show similar peaks appearing around 144,

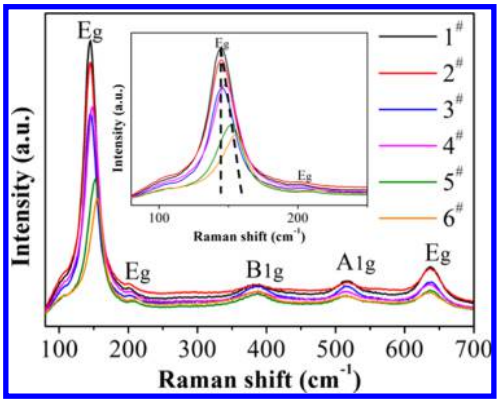

Figure 7. Raman spectra of anatase NTO thin films with different $\eta_{(004)}$. The inset depicts a high wave number shift of E_g peaks of NTO thin films from $1^{\#}$ to $6^{\#}$.

197, 399, 513, and 639 cm^{-1}, which correspond to three Raman modes of anatase TiO_2.[52−54] Raman experiments further confirm that NTO thin films do not exhibit any structural phase transition from anatase to rutile, and no NbO_x phases are observed either. This is in good agreement with our XRD analysis.

Raman peaks of NTO thin film $1^{\#}$ appear at 144 cm^{-1} (E_g), 199 cm^{-1} (E_g), 390 cm^{-1} (B_{1g}), 517 cm^{-1} (A_{1g}), and 638 cm^{-1} (E_g). Comparatively, Raman peaks of NTO thin film $6^{\#}$ appear at 154 cm^{-1} (E_g), 210 cm^{-1} (E_g), 387 cm^{-1} (B_{1g}), 514 cm^{-1} (A_{1g}), and 637 cm^{-1} (E_g). Compared to that of pure TiO_2, the B_{1g} mode (around 388 cm^{-1}) exhibits a slight shift to lower wavenumbers.[53] This slight change is attributed to the incorporation of substitutional niobium dopants.[55] Furthermore, as the (004)-oriented growth becomes stronger, the E_g mode (around 144 cm^{-1}) is further blue-shifted (the inset of Figure 7). According to previous research, the incorporation of substitutional niobium dopants have no contribution to Raman blue shift.[56] Therefore, we deduce that Raman blue shift of NTO films is attributed to the (004)-oriented growth. In addition, it is noted that the intensity of all of E_g mode peaks reduces gradually. The enhanced intensity of the Raman peak for $4^{\#}$ may be caused from good crystallinity.[57]

DOI: 10.1021/acsami.7b06792
ACS Appl. Mater. Interfaces XXXX, XXX, XXX−XXX

Physical Properties. The electrical properties of NTO thin films were characterized by the standard four-probe Hall effect measurements. The Hall effect measurements indicate that NTO films displayed n-type conductivity, with electrons being the dominant charge carrier species. The resistivity of as-grown thin films is too high for Hall effect measurements, so a rough analysis indicates a resistance of about 0.7−5 MΩ using a two-point probe of Agilent Millimeter. After annealing with Ar/H_2 (95:5, *v*/*v*), the resistance decreases drastically because of the reduction of charge carrier grain boundary scattering due to good crystallization of thin films. After annealing, the thickness of these thin films is between 590 and 640 nm (Figure S6).

As listed in Table 2, the sheet resistance of NTO thin film 1# is 76.9 Ω sq^{-1}, with a resistivity of 4.8×10^{-3} Ω cm, a Hall mobility of 1.1 cm^2 V^{-1} s^{-1}, and a charge carrier concentration of 1.2×10^{21} cm^{-3}. When $\eta_{(004)}$ increases, a dramatic improvement in electrical performance is observed due to the increase in Hall mobility. The Hall mobility of 2.1 cm^2 V^{-1} s^{-1} is confirmed as expected. The improvement of Hall mobility is due to the fact that the static effective mass, *m**, along the *a* axis ($m_{(100)}$*) is lesser than that along the *c* axis ($m_{(001)}$*).[31] In our work, a Hall mobility of 3.4 cm^2 V^{-1} s^{-1} is gained for NTO films with the highest $\eta_{(004)}$, which is about 3.1 times that of NTO film 1#. Furthermore, a charge carrier concentration of 2.9×10^{21} cm^{-3} is measured for NTO film 6#, which is nearly 2.4 times as large as that of NTO film 1#. Therefore, a low sheet resistance of 10.3 Ω sq^{-1} with a resistivity of 6.4×10^{-4} Ω cm is gained. These results suggest that electrical transport in NTO thin films is so anisotropic that it affects the conductivity of thin films with different $\eta_{(004)}$ values. Among these thin films, NTO thin films with the highest $\eta_{(004)}$ show better electrical performance than others.

Table 2. Electrical Properties of NTO Thin Films

sample	sheet resistance (Ω sq^{-1})	ρ (Ω cm)	μ (cm^2 V^{-1} s^{-1})	N (cm^{-3})
1#	76.9	4.8×10^{-3}	1.1	1.2×10^{21}
2#	36.0	2.3×10^{-3}	2.1	1.4×10^{21}
3#	24.8	1.5×10^{-3}	2.4	1.7×10^{21}
4#	19.9	1.2×10^{-3}	2.7	1.9×10^{21}
5#	11.5	7.1×10^{-4}	3.3	2.7×10^{21}
6#	10.3	6.4×10^{-4}	3.4	2.9×10^{21}

It is well known that high infrared radiation (IR) transmittance makes NTO thin films distinguished from traditional TCO thin films.[58] As shown in Figure 8a, D(101) NTO films (e.g., 1#) show high transmittance in the visible and near-infrared regions. As the $\eta_{(004)}$ increases, the near-IR transmittance gradually reduces. The light above the 1500 nm wavelength filters through a little for NTO films 5# and 6#. It should be noted that the starting wavelength for near-IR transmittance reduction shows a gradual blue shift as the $\eta_{(004)}$ increases. Black crosses are marked for reference (Figure 8a). According to the Drude model, IR transparency depends on the plasma frequency

$$\omega_p = \sqrt{\frac{Ne^2}{\varepsilon_0 m^*}} \quad (2)$$

where *N* is the charge carrier concentration, *e* is the charge, ε_0 is the free space permittivity, and *m** is the effective free electron mass.[58−60] Therefore, increasing charge carrier density and decreasing charge carrier effective mass are two approaches to increase the plasma resonance frequency and make resonance

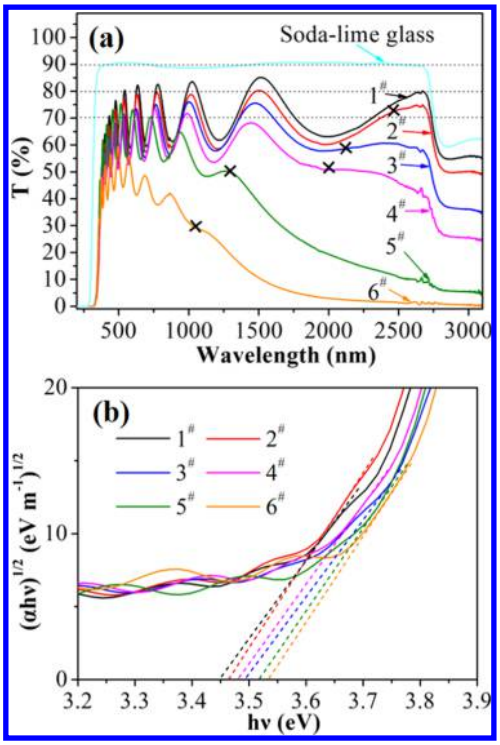

Figure 8. (a) Optical transmittance (*T*) for anatase NTO thin films with different $\eta_{(004)}$ values on a soda-lime glass. The light cyan line shows transmittance of the soda-lime glass substrate. The black cross on the curve of 2#−6# depicts the blue shift of the beginning of transmittance reduction for the curve compared to that of the prior. (b) Tauc's plots between $(\alpha h\nu)^{1/2}$ vs $h\nu$ for anatase NTO thin films with different $\eta_{(004)}$ values.

absorption effect blue shifted. In our work, anatase NTO thin films with a higher $\eta_{(004)}$ have a larger charge carrier density and a smaller charge carrier effective mass, which will result in further blue shift of reduction of transmittance in the near-IR region. These results suggest that anatase NTO thin films are optically anisotropic. This tunable IR transmittance would make NTO thin films applicable in optical glass and IR devices compared with traditional TCO thin films.

As shown in Figure 8b, the indirect bandgaps are determined by constructing Tauc plots using the $(\alpha h\nu)^{1/2}$ relation for NTO thin films. The values of Tauc's gap (E_g) are evaluated from the extrapolation of high-energy points to intercept on the energy axis with zero absorption. These bandgaps range slightly from 3.45 eV for NTO film 1# to 3.53 eV for NTO film 6#.

CONCLUSIONS

In conclusion, NTO thin films with different fractions of preferential (004) orientation ($\eta_{(004)}$) are successfully prepared by adjusting direct current sputtering parameters. A fascinating local-ordering of ions-packing phenomenon following the direction of the plasma beam was observed by SEM characterization, which was identified as the origin for achieving NTO films with different $\eta_{(004)}$ values. The electrical and optical properties present significant $\eta_{(004)}$-dependent anisotropy. The resistivity and sheet resistance of D(004) NTO thin films are as low as 6.4×10^{-4} Ω cm and 10.3 Ω sq^{-1}, respectively, making it a potential candidate for commercial TCO films. Gradual variation of near-infrared transmittance of NTO thin films is observed, which could be ascribed to the different charge carrier densities and charge carrier effective masses due to their different $\eta_{(004)}$

DOI: 10.1021/acsami.7b06792
ACS Appl. Mater. Interfaces XXXX, XXX, XXX−XXX

values. This property makes NTO thin films different from conventional TCOs, and thus could introduce some special functions in optical and optoelectronic applications. In summary, NTO thin films with high conductivity and tunable near-infrared transmittance would be appreciated as a multifunctional material in electrical, optical, and optoelectronic applications.

■ ASSOCIATED CONTENT

Supporting Information

The Supporting Information is available free of charge on the ACS Publications website at DOI: 10.1021/acsami.7b06792.

Additional electrical properties of reported NTO thin films, simulated calculation of the (004) and (101) planes, the residual stress of NTO films, photographs and optical transmittance for NTO thin films, Rietveld refinement and EDS data of NTO thin films $1^{\#}$–$6^{\#}$, and the thickness of NTO thin films (PDF)

■ AUTHOR INFORMATION

Corresponding Authors

*E-mail: liangjun@pkusz.edu.cn (J.L.).
*E-mail: panfeng@pkusz.edu.cn. Tel: 86-755-26033200 (F.P.).

ORCID

Feng Pan: 0000-0002-8216-1339

Notes

The authors declare no competing financial interest.

■ ACKNOWLEDGMENTS

X.Y. would like to thank Professor Guofu Wang in FJIRSM Institute for the valuable discussion on crystal growth, Engineer Shaojie Fu and Chunyan Song in Test Center of School of Advanced Materials of Peking University Shenzhen Graduate School for the valuable discussion on crystallization and assistance in SEM measurements, and Dr. Shuankui Li in School of Advanced Materials of Peking University Shenzhen Graduate School for valuable discussion on crystal growth in thin films. The authors gratefully acknowledge the financial support from the Shenzhen Key Science and Technology Plan (Grant No. JSGG20141118144410953), the Guangdong applied technology research special project (Grant No. 2015B090927003), Shenzhen Science and Technology Innovation Committee Grant (Grant No. JCYJ20150331101121646), and National Natural Science Foundation of China (51602010).

■ REFERENCES

(1) Zhang, L.; Zhou, Y.; Guo, L.; Zhao, W.; Barnes, A.; Zhang, H. T.; Eaton, C.; Zheng, Y.; Brahlek, M.; Haneef, H. F.; et al. Correlated Metals as Transparent Conductors. *Nat. Mater.* **2016**, *15*, 204–210.

(2) LebensHiggins, Z.; Scanlon, D. O.; Paik, H.; Sallis, S.; Nie, Y.; Uchida, M.; Quackenbush, N. F.; Wahila, M. J.; Sterbinsky, G. E.; Arena, D. A. Direct Observation of Electrostatically Driven Band Gap Renormalization in a Degenerate Perovskite Transparent Conducting Oxide. *Phys. Rev. Lett.* **2016**, *116*, No. 027602.

(3) Morales-Masis, M.; Dauzou, F.; Jeangros, Q.; Dabirian, A.; Lifka, H.; Gierth, R.; Ruske, M.; Moet, D.; Hessler-Wyser, A.; Ballif, C. An Indium-Free Anode for Large-Area Flexible OLEDs: Defect-Free Transparent Conductive Zinc Tin Oxide. *Adv. Funct. Mater.* **2016**, *26*, 384–392.

(4) Zeumault, A.; Subramanian, V. Mobility Enhancement in Solution-Processed Transparent Conductive Oxide TFTs due to Electron Donation from Traps in High-K Gate Dielectrics. *Adv. Funct. Mater.* **2016**, *26*, 955–963.

(5) Nayak, P. K.; Wang, Z.; Alshareef, H. N. Indium-Free Fully Transparent Electronics Deposited Entirely by Atomic Layer Deposition. *Adv. Mater.* **2016**, *28*, 7736–7744.

(6) Kim, D. J.; Kim, H. J.; Seo, K. W.; Kim, K. H.; Kim, T. W.; Kim, H. K. Indium-Free, Highly Transparent, Flexible $Cu_2O/Cu/Cu_2O$ Mesh Electrodes for Flexible Touch Screen Panels. *Sci. Rep.* **2015**, *5*, No. 16838.

(7) Göbelt, M.; Keding, R.; Schmitt, S. W.; Hoffmann, B.; Jäckle, S.; Latzel, M.; Radmilović, V. V.; Radmilović, V. R.; Spiecker, E.; Christiansen, S. Encapsulation of Silver Nanowire Networks by Atomic Layer Deposition for Indium-Free Transparent Electrodes. *Nano Energy* **2015**, *16*, 196–206.

(8) Jeon, I.; Nakao, S.; Hirose, Y.; Hasegawa, T.; Matsuo, Y. Indium-Free Inverted Organic Solar Cells Using Niobium-Doped Titanium Oxide with Integrated Dual Function of Transparent Electrode and Electron Transport Layer. *Adv. Electron. Mater.* **2016**, *2*, No. 1500341.

(9) Lu, L.; Guo, M.; Thornley, S.; Han, X.; Hu, J.; Thwaites, M. J.; Shao, G. Remote Plasma Sputtering Deposited Nb-Doped TiO_2 with Remarkable Transparent Conductivity. *Sol. Energy Mater. Sol. Cells* **2016**, *149*, 310–319.

(10) Bhachu, D. S.; Sathasivam, S.; Sankar, G.; Scanlon, D. O.; Cibin, G.; Carmalt, C. J.; Parkin, I. P.; Watson, G. W.; Bawaked, S. M.; Obaid, A. Y.; Al-Thabaiti, S.; Basahel, S. N. Solution Processing Route to Multifunctional Titania Thin Films: Highly Conductive and Photcatalytically Active Nb:TiO_2. *Adv. Funct. Mater.* **2014**, *24*, 5075–5085.

(11) Yamada, N.; Shibata, T.; Taira, K.; Hirose, Y.; Nakao, S.; Huong Hoang, N. L.; Hitosugi, T.; Shimada, T.; Sasaki, T.; Hasegawa, T. Enhanced Carrier Transport in Uniaxially (001)-Oriented Anatase $Ti_{0.94}Nb_{0.06}O_2$ Films Grown on Nanosheet Seed Layers. *Appl. Phys. Express* **2011**, *4*, No. 045801.

(12) Chen, B. X.; Rao, H. S.; Li, W. G.; Xu, Y. F.; Chen, H. Y.; Kuang, D. Bin; Su, C. Y. Achieving High-Performance Planar Perovskite Solar Cell with Nb-Doped TiO_2 Compact Layer by Enhanced Electron Injection and Efficient Charge Extraction. *J. Mater. Chem. A* **2016**, *4*, 5647–5653.

(13) Wang, H. Y.; Chen, J.; Xiao, F. X.; Zheng, J.; Liu, B. Doping-Induced Structural Evolution from Rutile to Anatase: Formation of Nb-Doped Anatase TiO_2 Nanosheets with High Photocatalytic Activity. *J. Mater. Chem. A* **2016**, *4*, 6926–6932.

(14) Furubayashi, Y.; Hitosugi, T.; Yamamoto, Y.; Inaba, K.; Kinoda, G.; Hirose, Y.; Shimada, T.; Hasegawa, T. A Transparent Metal: Nb-Doped Anatase TiO_2. *Appl. Phys. Lett.* **2005**, *86*, No. 252101.

(15) Yamada, N.; Hitosugi, T.; Kasai, J.; Hoang, N. L. H.; Nakao, S.; Hirose, Y.; Shimada, T.; Hasegawa, T. Direct Growth of Transparent Conducting Nb-Doped Anatase TiO_2 Polycrystalline Films on Glass. *J. Appl. Phys.* **2009**, *105*, No. 123702.

(16) Hitosugi, T.; Ueda, A.; Nakao, S.; Yamada, N.; Furubayashi, Y.; Hirose, Y.; Konuma, S.; Shimada, T.; Hasegawa, T. Transparent Conducting Properties of Anatase $Ti_{0.94}Nb_{0.06}O_2$ Polycrystalline Films on Glass Substrate. *Thin Solid Films* **2008**, *516*, 5750–5753.

(17) Seeger, S.; Ellmer, K.; Weise, M.; Gogova, D.; Abou-Ras, D.; Mientus, R. Reactive Magnetron Sputtering of Nb-Doped TiO_2 Films: Relationships between Structure, Composition and Electrical Properties. *Thin Solid Films* **2016**, *605*, 44–52.

(18) Wan, G.; Wang, S.; Zhang, X.; Huang, M.; Zhang, Y.; Duan, W.; Yi, L. Transparent Conductive Nb-Doped TiO_2 Films Deposited by RF Magnetron Co-Sputtering. *Appl. Surf. Sci.* **2015**, *357*, 622–625.

(19) Oka, N.; Sanno, Y.; Jia, J.; Nakamura, S.; Shigesato, Y. Transparent Conductive Nb-Doped TiO2 Films Deposited by Reactive Dc Sputtering Using Ti-Nb Alloy Target, Precisely Controlled in the Transition Region Using Impedance Feedback System. *Appl. Surf. Sci.* **2014**, *301*, 551–556.

(20) Hung, K. H.; Lee, P. W.; Hsu, W. C.; Hsing, H. C.; Chang, H. T.; Wong, M. S. Transparent Conducting Oxide Films of Heavily Nb-Doped Titania by Reactive Co-Sputtering. *J. Alloys Compd.* **2011**, *509*, 10190–10194.

(21) Kasai, J.; Hitosugi, T.; Moriyama, M.; Goshonoo, K.; Hoang, N. L. H.; Nakao, S.; Yamada, N.; Hasegawa, T. Properties of TiO_2-Based

DOI: 10.1021/acsami.7b06792
ACS Appl. Mater. Interfaces XXXX, XXX, XXX–XXX

Transparent Conducting Oxide Thin Films on GaN(0001) Surfaces. *J. Appl. Phys.* **2010**, *107*, No. 053110.
(22) Yamada, N.; Hitosugi, T.; Kasai, J.; Hoang, N. L. H.; Nakao, S.; Hirose, Y.; Shimada, T.; Hasegawa, T. Transparent Conducting Nb-Doped Anatase TiO_2 (TNO) Thin Films Sputtered from Various Oxide Targets. *Thin Solid Films* **2010**, *518*, 3101−3104.
(23) Sato, Y.; Akizuki, H.; Kamiyama, T.; Shigesato, Y. Transparent Conductive Nb-Doped TiO_2 Films Deposited by Direct-Current Magnetron Sputtering Using a TiO_{2-X} Target. *Thin Solid Films* **2008**, *516*, 5758−5762.
(24) Gillispie, M. A.; Van Hest, M. F. A. M.; Dabney, M. S.; Perkins, J. D.; Ginley, D. S. Rf Magnetron Sputter Deposition of Transparent Conducting Nb-Doped TiO_2 Films on $SrTiO_3$. *J. Appl. Phys.* **2007**, *101*, No. 033125.
(25) Niemelä, J. P.; Hirose, Y.; Hasegawa, T.; Karppinen, M. Transition in Electron Scattering Mechanism in Atomic Layer Deposited Nb:TiO_2 Thin Films. *Appl. Phys. Lett.* **2015**, *106*, No. 042101.
(26) Duta, M.; Simeonov, S.; Teodorescu, V.; Predoana, L.; Preda, S.; Nicolescu, M.; Marin, A.; Spasov, D.; Gartner, M.; Zaharescu, M. Structural and Electrical Properties of Nb Doped TiO_2 Films Prepared by the Sol-gel Layer-by-Layer Technique. *Mater. Res. Bull.* **2016**, *74*, 15−20.
(27) Lu, Y.; Khan, S.; Song, C. L.; Wang, K. K.; Yuan, G. Z.; Li, W.; Han, G. R.; Liu, Y. Doping Concentration Effects upon Column-Structured Nb:TiO_2 for Transparent Conductive Thin Films Prepared by a Sol-gel Method. *J. Alloys Compd.* **2016**, *663*, 413−418.
(28) Depla, D.; De Gryse, R. Target Poisoning during Reactive Magnetron Sputtering: Part I: The Influence of Ion Implantation. *Surf. Coat. Technol.* **2004**, *183*, 184−189.
(29) Depla, D.; De Gryse, R. Target Poisoning during Reactive Magnetron Sputtering: Part II: The Influence of Chemisorption and Gettering. *Surf. Coat. Technol.* **2004**, *183*, 190−195.
(30) Depla, D.; De Gryse, R. Target Poisoning during Reactive Magnetron Sputtering: Part III: The Prediction of the Critical Reactive Gas Mole Fraction. *Surf. Coat. Technol.* **2004**, *183*, 196−203.
(31) Hirose, Y.; Yamada, N.; Nakao, S.; Hitosugi, T.; Shimada, T.; Hasegawa, T. Large Electron Mass Anisotropy in a D-Electron-Based Transparent Conducting Oxide: Nb-Doped Anatase TiO_2 Epitaxial Films. *Phys. Rev. B: Condens. Matter Mater. Phys.* **2009**, *79*, No. 165108.
(32) Gong, X. Q.; Selloni, A.; Batzill, M.; Diebold, U. Steps on Anatase TiO_2 (101). *Nat. Mater.* **2006**, *5*, 665−670.
(33) Shibata, T.; Fukuda, K.; Ebina, Y.; Kogure, T.; Sasaki, T. One-Nanometer-Thick Seed Layer of Unilamellar Nanosheets Promotes Oriented Growth of Oxide Crystal Films. *Adv. Mater.* **2008**, *20*, 231−235.
(34) Stefanov, B. I.; Niklasson, G. A.; Granqvist, C. G.; Osterlund, L. Quantitative Relation between Photocatalytic Activity and Degree of ⟨001⟩ Orientation for Anatase TiO_2 Thin Films. *J. Mater. Chem. A* **2015**, *3*, 17369−17375.
(35) Zheng, J. Y.; Bao, S.; Guo, Y.; Jin, P. Anatase TiO_2 Films with Dominant {001} Facets Fabricated by Direct-Current Reactive Magnetron Sputtering at Room Temperature: Oxygen Defects and Enhanced Visible-Light Photocatalytic Behaviors. *ACS Appl. Mater. Interfaces* **2014**, *6*, 5940−5946.
(36) Ligorio, G.; Nardi, M. V.; Koch, N. Lithography-Free Miniaturization of Resistive Nonvolatile Memory Devices to the 100 nm Scale by Glancing Angle Deposition. *Nano Lett.* **2017**, *17*, 1149−1153.
(37) Hou, Y.; Leung, H. M.; Chan, C. T.; Du, J.; Chan, H. L.; Lei, D. Y. Ultrabroadband Optical Superchirality in a 3D Stacked-Patch Plasmonic Metamaterial Designed by Two-Step Glancing Angle Deposition. *Adv. Funct. Mater.* **2016**, *26*, 7807−7816.
(38) Sanchez-Valencia, J. R.; Longtin, R.; Rossell, M. D.; Groening, P. Growth Assisted by Glancing Angle Deposition (GAGLAD): A New Technique to Engineer Highly Porous Anisotropic Thin Films. *ACS Appl. Mater. Interfaces* **2016**, *8*, 8686−8693.
(39) Zhou, Y.; Taima, T.; Miyadera, T.; Yamanari, T.; Kitamura, M.; Nakatsu, K.; Yoshida, Y. Glancing Angle Deposition of Copper Iodide Nanocrystals for Efficient Organic Photovoltaics. *Nano Lett.* **2012**, *12*, 4146−4152.
(40) Garcíamartín, J. M.; Alvarez, R.; Romerogómez, P.; Cebollada, A.; Palmero, A. Tilt Angle Control of Nanocolumns Grown by Glancing Angle Sputtering at Variable Argon Pressures. *Appl. Phys. Lett.* **2010**, *97*, No. 173103.
(41) Wade, R. H.; Silcox, J. Small Angle Electron Scattering from Vacuum Condensed Metallic Films II. Experimental Results. *Phys. Status Solidi B* **1967**, *19*, 63−76.
(42) Wang, C.; Li, J.; Dho, J. Post-Deposition Annealing Effects on the Transparent Conducting Properties of Anatase Nb:TiO_2 Films on Glass Substrates. *Mater. Sci. Eng., B* **2014**, *182*, 1−5.
(43) Llordés, A.; Garcia, G.; Gazquez, J.; Milliron, D. J. Tunable near-Infrared and Visible-Light Transmittance in Nanocrystal-in-Glass Composites. *Nature* **2013**, *500*, 323−326.
(44) Schubert, A.; Kämpfe, B.; Ermrich, M.; Auerswald, E.; Tränkner, K. Use of an X-Ray Imaging Plate for Stress Analysis. *Mater. Sci. Forum* **1994**, *166-169*, 151−156.
(45) Borgese, L.; Gelfi, M.; Bontempi, E.; Goudeau, P.; Geandier, G.; Thiaudière, D.; Depero, L. E. Young modulus and Poisson ratio measurements of TiO_2, thin films deposited with atomic layer deposition. *Surf. Coat. Technol.* **2012**, *206*, 2459−2463.
(46) Hoffman, D. W.; Thornton, J. A. Compressive stress and inert gas in Mo films sputtered from a cylindrical-post magnetron with Ne, Ar, Kr, and Xe. *J. Vac. Sci. Technol.* **1980**, *17*, 380−383.
(47) Hoffman, D. W.; Kukla, C. M. Determination of film stresses during sputter deposition using an in situ probe. *J. Vac. Sci. Technol., A* **1985**, *3*, 2600−2604.
(48) Boulestelx, C.; Kang, Z.; Lottiaux, M. HREM study of crystalline and amorphous regions of a TiO_2 thin layer: Modification of the lattice parameter inside small clusters. *Phys. Status Solidi A* **1986**, *94*, 499−506.
(49) Scanlon, D. O.; Dunnill, C. W.; Buckeridge, J.; Shevlin, S. A.; Logsdail, A. J.; Woodley, S. M.; Catlow, C. R. A.; Powell, M. J.; Palgrave, R. G.; Parkin, I. P.; Watson, G. W.; Keal, T. W.; Sherwood, P.; Walsh, A.; Sokol, A. A. Band Alignment of Rutile and Anatase TiO_2. *Nat. Mater.* **2013**, *12*, 798−801.
(50) Kafizas, A.; Dunnill, C.; Parkin, I. Combinatorial Atmospheric Pressure Chemical Vapour Deposition (cAPCVD) of Niobium Doped Anatase; Effect of Niobium on the Conductivity and Photocatalytic Activity. *J. Mater. Chem.* **2010**, *20*, 8336−8349.
(51) Fujishima, A.; Honda, K. Electrochemical Photolysis of Water at a Semiconductor Electrode. *Nature* **1972**, *238*, 37−38.
(52) Mulmi, D. D.; Sekiya, T.; Kamiya, N.; Kurita, S.; Murakami, Y.; Kodaira, T. Optical and Electric Properties of Nb-Doped Anatase TiO_2 Single Crystal. *J. Phys. Chem. Solids* **2004**, *65*, 1181−1185.
(53) Ohsaka, T.; Izumi, F.; Fujiki, Y. Raman Spectrum of Anatase, TiO_2. *J. Raman Spectrosc.* **1978**, *7*, 321−324.
(54) Beattie, I. R.; Gilson, T. R. Single Crystal Laser Raman Spectroscopy. *Proc. R. Soc. London, Ser. A* **1968**, *307*, 407−429.
(55) Koozegar, B.; Sarraf-mamoory, R.; Fujishima, A. Influence of Nb Dopant on the Structural and Optical Properties of Nanocrystalline TiO_2 Thin Films. *Mater. Chem. Phys.* **2012**, *132*, 210−215.
(56) Yang, M.; Hume, C.; Lee, S.; Son, Y. H.; Lee, J. K. Correlation between Photocatalytic Efficacy and Electronic Band Structure in Hydrothermally Grown TiO_2 Nanoparticles. *J. Phys. Chem. C* **2010**, *114*, 15292−15297.
(57) Shirai, K.; Moriguchi, Y.; Ichimura, M.; Usami, A.; Saji, M. Relationship between Raman Spectra and Crystallinity of CdS Films Grown by Cathodic Electrodeposition. *Jpn. J. Appl. Phys., Part 1* **1996**, *35*, 2057−2060.
(58) Su, W.; Song, K.; Huo, D.; Li, B. Analysis of Correlation between Electrical and Infrared Optical Properties of Anatase Nb Doped TiO_2 Films. *Curr. Appl. Phys.* **2013**, *13*, 556−561.
(59) Gupta, R. K.; Ghosh, K.; Mishra, S. R.; Kahol, P. K. High Mobility Ti-Doped In_2O_3 Transparent Conductive Thin Films. *Mater. Lett.* **2008**, *62*, 1033−1035.
(60) Fujiwara, H. *Spectroscopic Ellipsometry: Principles and Applications*; Wiley, New York, 2007.

DOI: 10.1021/acsami.7b06792
ACS Appl. Mater. Interfaces XXXX, XXX, XXX−XXX